The Meteoritical Society

Meteoritics & Planetary Science 54, Nr 9, 1907–1918 (2019)
doi: 10.1111/maps.13349

A vacancy-rich, partially inverted spinelloid silicate, $(Mg,Fe,Si)_2(Si,\square)O_4$, as a major matrix phase in shock melt veins of the Tenham and Suizhou L6 chondrites

Chi MA [1*], Oliver TSCHAUNER [2], Luca BINDI[3,4], John R. BECKETT[1], and Xiande XIE[5,6]

[1]Division of Geological and Planetary Sciences, California Institute of Technology, Pasadena, California 91125, USA
[2]Department of Geoscience, University of Nevada, Las Vegas, Nevada 89154, USA
[3]Dipartimento di Scienze della Terra, Università degli Studi di Firenze, Via G. La Pira 4, I-50121 Firenze, Italy
[4]CNR, Istituto di Geoscienze e Georisorse, Sezione di Firenze, Via G. La Pira 4, I-50121 Firenze, Florence, Italy
[5]Key Laboratory of Mineralogy and Metallogeny, Guangzhou Institute of Geochemistry, Chinese Academy of Sciences, Guangzhou 510640, China
[6]Guangdong Provincial Key Laboratory of Mineral Physics and Materials, Chinese Academy of Sciences, Guangzhou 510640, China
[*]Corresponding author. E-mail: chi@gps.caltech.edu

(Received 21 December 2018; revision accepted 06 June 2019)

Abstract–A new high-pressure silicate, $(Mg,Fe,Si)_2(Si,\square)O_4$ with a tetragonal spinelloid structure, was discovered within shock melt veins in the Tenham and Suizhou meteorites, two highly shocked L6 ordinary chondrites. Relative to ringwoodite, this phase exhibits an inversion of Si coupled with intrinsic vacancies and a consequent reduction of symmetry. Most notably, the spinelloid makes up about 30–40 vol% of the matrix of shock veins with the remainder composed of a vitrified $(Mg,Fe)SiO_3$ phase (in Tenham) or $(Mg,Fe)SiO_3$-rich clinopyroxene (in Suizhou); these phase assemblages constitute the bulk of the matrix in the shock veins. Previous assessments of the melt matrices concluded that majorite and akimotoite were the major phases. Our contrasting result requires revision of inferred conditions during shock melt cooling of the Tenham and Suizhou meteorites, revealing in particular a much higher quench rate (at least 5×10^3 K s^{-1}) for veins of 100–500 μm diameter, thus overriding formation of the stable phase assemblage majoritic garnet plus periclase.

INTRODUCTION

Highly shocked meteorites and terrestrial impactites contain high-pressure minerals that are otherwise expected to occur in the deep Earth mantle, where they are generally inaccessible to mineralogical and petrographic study (Stöffler 1997). Indeed, the four rock-forming minerals dominating the Earth's transition zone and lower mantle (majorite, wadsleyite, ringwoodite, bridgmanite) were all originally discovered in shocked meteorites (Binns et al. 1969; Smith and Mason 1970; Price et al. 1983; Tschauner et al. 2014). Despite the very short duration of the stress pulses associated with shocked meteorites (e.g., Sharp and DeCarli 2006; Walton et al. 2014; Ma et al. 2016), almost none of the vast number of metastable high-pressure phases that have been synthesized in static or shock experiments are observed in natural shock-generated mineral assemblages. Iron-bearing akimotoite (Sharp et al. 1997; Tomioka and Fujino 1997; Ferroir et al. 2008; Tschauner et al. 2018) and the hollandite-type alkali-silicates (Gillet et al. 2000; Ma et al. 2018) are the known exceptions. All other observed high-pressure phases in meteorites are also stable phases at high pressure with stability fields under static pressure–temperature conditions, albeit, not necessarily under the pressure–temperature conditions imposed by a shock event.

Here, we report the discovery and characterization of a previously unknown spinelloid silicate (SPD) with a structural formula of $(Mg,Fe,Si)_2(Si,\square)O_4$ as a major constituent in the matrices of shock melt veins in two of

[Correction added on 16 August 2019 after first online publication: Table 2 content is replaced with correct data]

the most extensively studied, highly shocked ordinary chondrites, Tenham and Suizhou. The main structural characteristic of this new phase is the octahedral coordination of Si by oxygen in correlation with partially vacant tetrahedral sites. This polyhedral arrangement of Si (i.e., coexisting four- and six-coordinated Si) may be relevant for the local structure of partial melts in the 15–25 GPa regime in Earth's mantle (e.g., Mosenfelder et al. 2009).

It is generally assumed that matrices in shock melt veins from highly shocked chondrites are composed of majoritic garnet and akimotoite (Sharp et al. 1997; Tomioka and Fujino 1997; Ferroir et al. 2008). Akimotoite, a high-pressure polymorph of $MgSiO_3$ in the ilmenite structure (Tomioka and Fujino 1997, 1999), has a stability field narrowly limited to near endmember compositions by the stability fields of ringwoodite or wadsleyite plus stishovite (e.g., Fabrichnaya 1995). In Tenham and Suizhou, as well as other highly shocked chondrites, however, akimotoite can contain 5–7 mole% hemleyite, the Fe-analog of akimotoite, and values exceeding 50% $FeSiO_3$ component have been observed (Bindi et al. 2017) despite the lack of thermodynamic stability relative to other phases (Sharp et al. 1997; Tomioka and Fujino 1999; Tschauner et al. 2018). This reflects the metastable formation of solid phases during a shock-compression state where there is insufficient time for nucleation and growth of the stable phase assemblage. Akimotoite has been reported as a major quench phase in the shock melt matrix of the Acfer 040 L6 chondrite (Sharp et al. 1997) and as aggregates that replace clasts of enstatite trapped in shock melt veins (Tomioka and Fujino 1997; Tschauner et al. 2014, 2018). The latter type of occurrence clearly reflects kinetic effects: larger clasts contain cores of untransformed enstatite with rims of akimotoite (Ferroir et al. 2008), whereas smaller clasts are transformed into akimotoite or assemblages containing akimotoite and bridgmanite (Tschauner et al. 2014). Occurrences of akimotoite within the matrices of shock melt veins of Acfer 040 (Sharp et al. 1997) imply that, despite the high temperatures, shock melt crystallization is nevertheless also controlled by kinetic effects. This type of occurrence has not been observed in other highly shocked L6 chondrites such as Tenham (Ferroir et al. 2008; Tschauner et al. 2018), where akimotoite is rare within shock melt vein matrices rather than a major component (Tschauner et al. 2018). Similar considerations apply to majorite, which was recently found as rare fragments in the shock vein of the Tenham meteorite (due to transformation of low-Ca pyroxene), together with olivine and plagioclase transformed into ringwoodite and diaplectic glass (Tomioka et al. 2016). Abundant crystallites of $(Mg,Fe)SiO_3$ in the melt vein matrix in Tenham have been interpreted as majoritic garnet despite the absence of a significant contribution to diffraction patterns from this presumed majoritic garnet in the melt matrix (Mori 1994; Tomioka and Fujino 1997; Tschauner et al. 2014).

There is a fundamental discrepancy in the literature concerning the mineralogy of shock melt matrices, as outlined above, and this translates into fundamental differences in inferred thermal histories. Here, we present the results of analysis of the matrices of shock melt veins in the highly shocked Tenham and Suizhou L6 chondrites and show that they contain neither akimotoite nor majoritic garnet. The matrices are composed of a spinelloid silicate, $(Mg,Fe,Si)_2(Si,\square)O_4$, and either a vitrified $(Mg,Fe)SiO_3$ phase (Tenham) or clinopyroxene (Suizhou).

SAMPLES AND ANALYTICAL METHODS

Studied Samples

Ordinary chondrites are a group of primitive meteorites that are subdivided into chemical classes (H, L, LL) and characterized by the degree of thermal and shock metamorphism. A variety of properties can be used to determine the chemical class, although none of these are universally applicable (see Jilly-Rehak et al. [2016] for a modern, multipronged approach to this problem). The chemical designation is combined with a number (3–6) corresponding to the degree of thermal metamorphism within the parent body, with 3.0 corresponding to no observable effects and higher numbers referring to greater intensity (Van Schmus and Wood 1967; Sears et al. 1980). The degree of shock metamorphism is characterized by a designation ranging from S1 (no observed shock effects) to S6 (highly shocked; Stöffler et al. 1991, 2018).

The 160 kg Tenham (L6) meteorite fell near Tenham station in western Queensland, Australia, in 1897 (Binns et al. 1969) and the ~70 kg Suizhou (L6) meteorite fell near the city of Suizhou in Hubei province, China, on April 15, 1986 (Wang and Rubin 1987). Both Tenham and Suizhou are fresh falls with strong shock features (S6) and, given the relatively large amount of available material, they have been heavily studied (e.g., Binns et al. 1969; Tomioka and Fujino 1997; Xie et al. 2001; Tschauner et al. 2014, 2018; Tomioka et al. 2016; Xie and Chen 2016; Bindi et al. 2017; and references therein), becoming de facto standards for comparison in the study of shock features in other meteorites and in experiments (e.g., Chen et al. 2002, 2004a; Hu and Sharp 2017).

The new spinelloid silicate was identified in sections USNM 7703 from Tenham and SCM1 and MSN3238/I from Suizhou (Figs. 1–3). USNM 7703, prepared at Caltech and deposited in the collections of the

Smithsonian Institution's National Museum of Natural History, also hosts type bridgmanite ([Mg,Fe]SiO_3-perovskite) (Tschauner et al. 2014). SCM1 is a Suizhou section at Caltech, originally prepared at the China University of Geosciences (Wuhan). MSN3238/I was prepared at the University of Firenze (Italy) and deposited in the collections of the Museo di Storia Naturale, University of Firenze (Italy). This section also hosts type hemleyite, the Fe-analog of akimotoite (Bindi et al. 2017), and shenzhuangite, the Ni-analog of chalcopyrite (Bindi and Xie 2018).

Analytical Methods

Electron probe microanalysis (EPMA), high-resolution scanning electron microscopy (SEM), electron backscatter diffraction (EBSD), and synchrotron X-ray diffraction and single-crystal X-ray diffraction analyses were used to determine the composition and structure of the new silicate and to characterize associated phases. Backscatter electron (BSE) imaging was performed using a ZEISS 1550VP field emission SEM at Caltech and a ZEISS EVO MA15 SEM at Università degli Studi di Firenze. EBSD analyses were performed using an HKL EBSD system on the ZEISS 1550VP SEM, operated at 20 kV and 6 nA in focused beam mode with a 70° tilted stage and variable pressure mode (25 Pa) using procedures described in Ma and Rossman (2008). The EBSD system was calibrated using a single-crystal silicon standard. Micro-Raman analysis was attempted with a Renishaw inVia™ Qontor Raman microscope using a green laser (512 nm) at 0.7 mW power in a confocal mode. The collected Raman spectra showed the features of multiple phases within the matrix and embedded clasts underneath the surface, so that no distinct feature of the spinelloid silicate could be identified.

Chemical analyses of the new silicate and associated minerals in Tenham section USNM 7703 and Suizhou section SCM1 were determined using a JEOL 8200 electron microprobe at Caltech (WDS: 10 kV; 5 nA; beam in focused mode for mineral analysis and a 5-μm defocused mode for bulk matrix analysis) interfaced with the Probe for EPMA program from Probe Software, Inc. The focused electron beam is ~120 nm in diameter with an interaction volume ~700 nm across at 10 kV, estimated using the Casino Monte Carlo simulation of electron trajectory in this spinelloid silicate (Fig. S3 in supporting information). Standards for analysis were anorthite (Si$K\alpha$, Al$K\alpha$, Ca$K\alpha$), albite (Na$K\alpha$), fayalite (Fe$K\alpha$), forsterite (Mg$K\alpha$), Mn_2SiO_4 (Mn$K\alpha$), TiO_2 (Ti$K\alpha$), Cr_2O_3 (Cr$K\alpha$), and microcline (K$K\alpha$). Electron beam damage to the new silicate and $MgSiO_3$ phases was not observed. Quantitative elemental microanalyses were processed with the CITZAF correction procedure (Armstrong 1995). An additional analysis on the new silicate was conducted on Suizhou section MSN3238/I

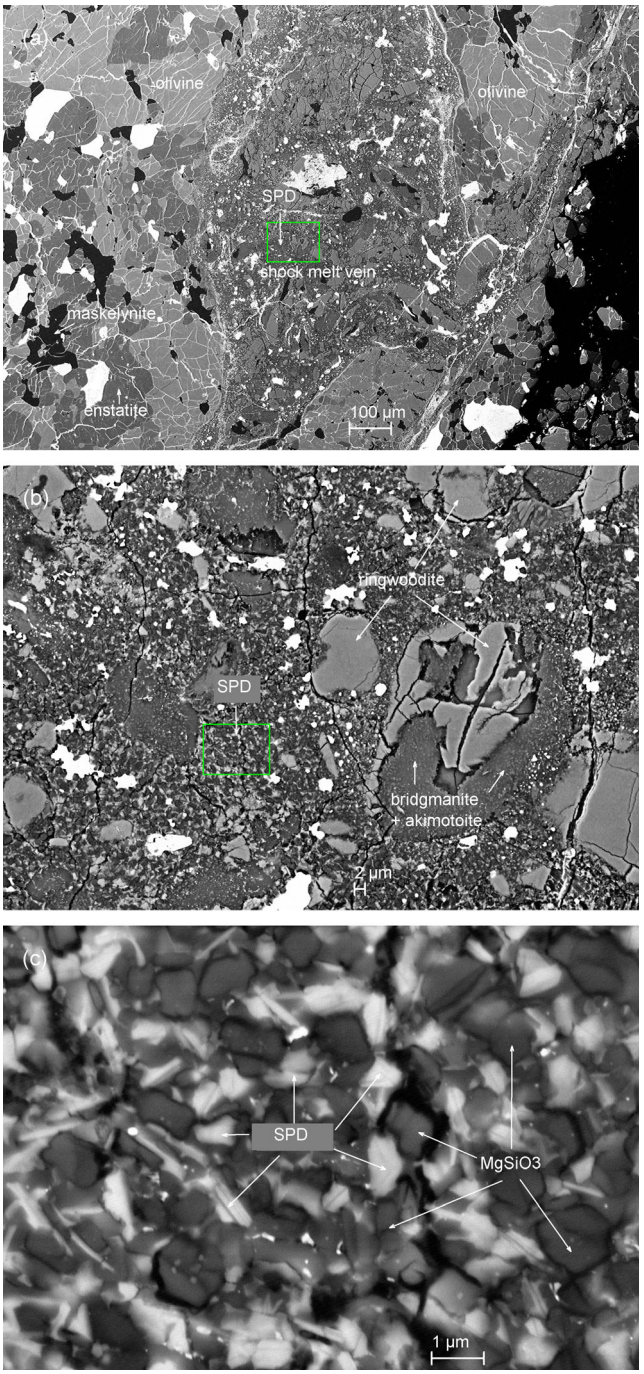

Fig. 1. SEM BSE images showing the spinelloid silicate (SPD) within a shock melt vein, in Tenham section USNM 7703, with a (Mg,Fe)SiO_3 phase in the vein matrix. a) Overview of vein and constituent phases. b) Enlarged view of rectangular area outlined in (a). c) Enlarged BSE image of rectangular region outlined in (b). (Color figure can be viewed at wile yonlinelibrary.com.)

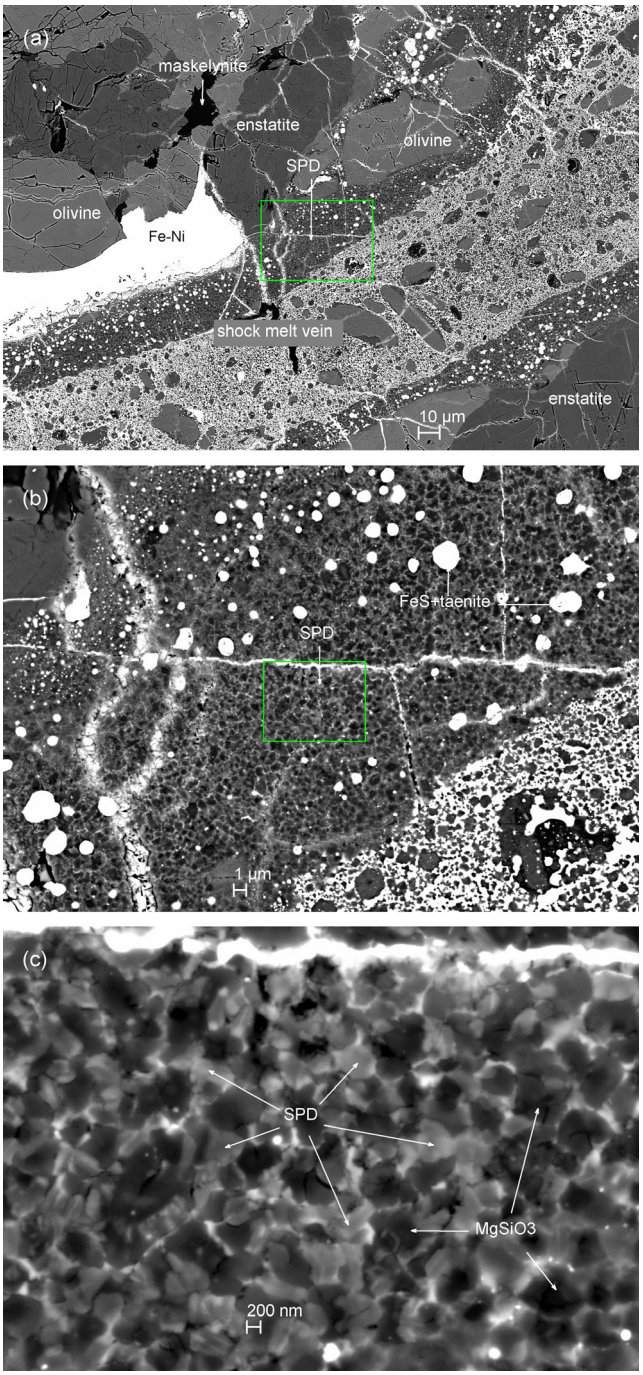

Fig. 2. BSE images showing fine-grained spinelloid with (Mg, Fe)SiO_3-clinopyroxene within the matrix of a melt vein in Suizhou section SCM1. The panels show progressively smaller scales. a) Overview. b) Enlarged BSE image of rectangular region outlined in (a). c) Enlarged BSE image of rectangular region outlined in (b). Crystal size of the SPD phase is generally in the range of 100–800 nm. (Color figure can be viewed at wileyonlinelibrary.com.)

using a JEOL JXA 8600 microprobe at the Dipartimento di Scienze della Terra, University of Florence, Italy (WDS mode, 15 kV, 10 nA, 1 μm beam

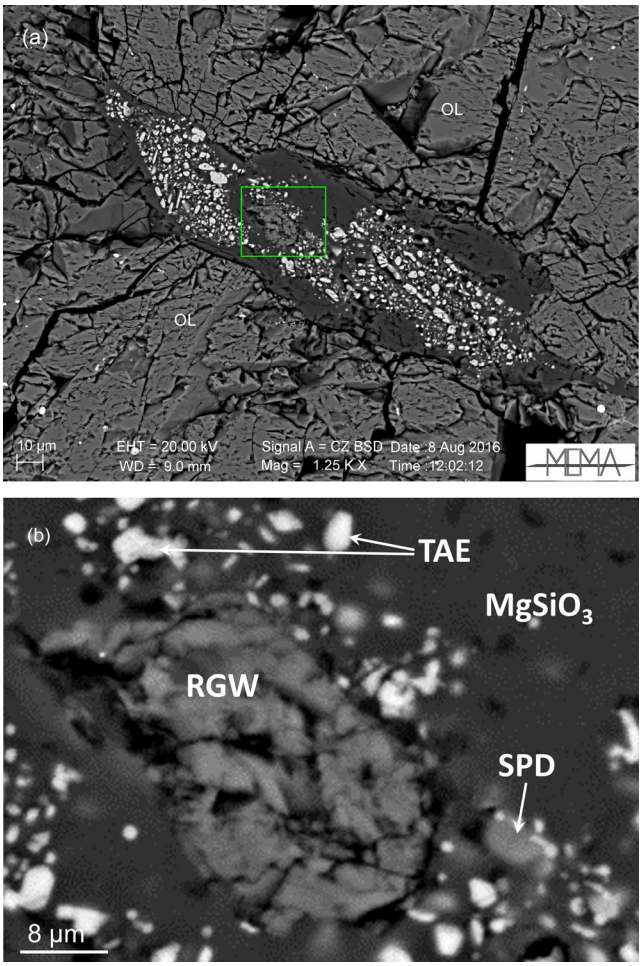

Fig. 3. BSE images showing one possible spinelloid grain in Suizhou section MSN3238/I. a) Overview of shock melt vein. OL = olivine. b) Close-up of area outlined by a rectangle in (a). The SPD grain is a single crystal, ~3 × 7 μm in size, along with a (Mg,Fe)SiO_3 phase, taenite (TAE), and ringwoodite (RGW) in a melt vein. (Color figure can be viewed at wileyonlinelibrary.com.)

size, and counting times of 20 s on peak and 10 s for background). The $K\alpha$ lines for all of the elements were used and the standards employed were albite (Na, Al, Si), synthetic Cr_2O_3 (Cr), ilmenite (Fe), olivine (Mg), diopside (Ca), sanidine (K), rutile (Ti), and bustamite (Mn). The chemical analyses are summarized in Table 1.

Synchrotron diffraction data were collected on Tenham section USNM 7703 at the undulator beamline 13-IDD (GSECARS, APS, Argonne National Laboratory) using a primary beam of wavelength 0.3344 Å, monochromatized by a double-crystal Si monochromator. The X-ray beam was focused to 2 × 3 μm^2 by vertical and horizontal Kirkpatrick–Baez mirrors of 200 mm focal length. A MAR165 CCD area detector was used for obtaining diffraction data, which were collected in forward scattering geometry.

Table 1. Compositions of the new spinelloid silicate (SPD), associated (Mg,Fe)SiO_3 phases and shock melt matrices in the Tenham and Suizhou meteorites.

	Tenham						Suizhou							
Constituent wt%	First occ. SPD in Fig. 1 n = 13	SD	$MgSiO_3$ (amorph) in Fig. 1 n = 9	SD	Bulk matrix in Fig. 1 n = 10	SD	Second occ. SPD in Fig. 2 n = 10	SD	$MgSiO_3$ (cpx) in Fig. 2 n = 10	SD	Bulk matrix in Fig. 2 n = 8	SD	Third occ. SPD in Fig. 3 n = 5	SD
SiO_2	41.98	1.61	53.15	0.69	49.54	0.93	44.32	0.62	52.16	0.76	47.19	1.17	42.04	0.21
TiO_2	0.12	0.04	0.1	0.01	0.11	0.08	0.09	0.06	0.09	0.04	0.12	0.03	0.03	0.02
Al_2O_3	2.23	0.18	4.15	0.26	3.72	0.24	3.53	0.11	3.95	0.31	3.73	0.20	2.08	0.17
FeO	27.73	1.81	9.73	0.51	14.95	1.19	16.96	0.47	11.41	0.95	16.96	0.85	28.55	0.51
MgO	24.85	0.64	29.12	0.99	26.92	0.87	32.42	1.1	28.11	1.13	27.67	1.17	23.9	0.78
CaO	2.04	0.36	1.5	0.4	2.65	0.29	1.09	0.13	1.23	0.25	1.35	0.12	2.15	0.15
Na_2O	0.85	0.1	0.92	0.13	1.57	0.19	1.31	0.11	1.39	0.33	1.76	0.37	1.03	0.12
K_2O	0.09	0.02	0.1	0.02	0.16	0.03	0.08	0.02	0.06	0.02	0.11	0.01	0.02	0.02
Cr_2O_3	0.27	0.09	0.25	0.04	0.29	0.10	0.52	0.08	0.42	0.09	0.41	0.08	0.4	0.12
MnO	0.15	0.1	0.29	0.04	0.35	0.08	0.34	0.06	0.31	0.08	0.35	0.09	0.08	0.03
Total	100.32		99.33		100.28		100.66		99.14		99.65		100.28	
No. O atoms	4		6		10		4		6		10		4	
Si	1.11		1.89		3.03		1.1		1.88		2.94		1.11	
Ti	0		0		0		0		0		0.01		0	
Al	0.07		0.17		0.27		0.1		0.17		0.27		0.06	
Fe^{2+}	0.61		0.29		0.77		0.35		0.34		0.88		0.63	
Mg	0.98		1.55		2.45		1.2		1.51		2.57		0.94	
Ca	0.06		0.06		0.17		0.03		0.05		0.09		0.06	
Na	0.04		0.06		0.19		0.06		0.1		0.21		0.05	
K	0		0		0.01		0		0		0.01		0	
Cr^{3+}	0.01		0.01		0.01		0.01		0.01		0.02		0.01	
Mn^{2+}	0		0.01		0.02		0.01		0.01		0.02		0	
Sum cations	2.88		4.04		6.93		2.86		4.07		7.02		2.86	

n = number of analyses; SD = one standard deviation of the mean based on all of the analyses; occ. = occurrence; amorph = amorphous; cpx = clinopyroxene.

Calibration was conducted with GSE-ADA (Dera et al. 2013) and DIOPTAS (Prescher and Prakapenka 2015). Integration and correction for geometric distortion were conducted with DIOPTAS, too. Unit cell dimensions; site occupancies; and the x-, y-, and z-fractional coordinates of O were refined using the Rietveld method and are given in Table 2.

Independent X-ray studies were performed at the CRIST, Centro di Studi per la Cristallografia Strutturale, Department of Chemistry, Università di Firenze, Italy, on a small fragment (size about 11 × 9 × 7 μm) that was extracted from the Suizhou MSN3238/I polished section under a reflected light microscope, and mounted on a 5-μm diameter carbon fiber, which was, in turn, attached to a glass rod. Data were collected with an Oxford Diffraction Xcalibur3 CCD single-crystal diffractometer using Mo$K\alpha$ radiation (λ = 0.71073 Å) with working conditions of 60 kV, 50 nA, and a 300 s exposure time per frame; the detector-to-sample distance was 6 cm. Data were integrated and corrected for standard Lorentz polarization factors with the CrysAlis RED package (Oxford Diffraction 2006) and for absorption correction with ABSPACK in CrysAlis RED (Oxford Diffraction 2006). A total of 199 unique reflections were collected.

RESULTS

Occurrence and Appearance

The new silicate occurs in the matrices of shock melt veins. In Tenham, it occurs with an amorphous (Mg,Fe)SiO_3-phase (Fig. 1; first occurrence). The crystalline habit of the vitrified phase indicates that it is not quenched melt but the result of vitrification of a formerly crystalline phase. In Tenham, shock melt veins are loaded with clasts of olivine, pyroxene, and feldspar from the host rock, which are partially to fully converted to ringwoodite, majorite; akimotoite; bridgmanite; lingunite; periclase; and, less commonly, clinopyroxene (e.g., Binns et al.

Table 2. Unit cell dimensions, fractional atom coordinates, site fractional occupancies, and isotropic thermal displacement factors of the new silicate with a tetragonal $I4_1/amd$ structure in Tenham (the first occurrence).

Atom	Wyckoff	Occupancy	x	y	z
Si1	4*a*	0.78 (1)	0	0	0
Mg1	4*a*	0.10 (2)	0	0	0
Mg2	16*h*	0.66 (4)	0.248 (1)	0	0.374 (3)
Fe	16*h*	0.14 (3)	0.248 (1)	0	0.374 (3)
Si2	16*h*	0.10 (4)	0.248 (1)	0	0.374 (3)
Al	16h	0.10 (6)	0.248 (1)	0	0.374 (3)
Ca	16*h*	0.05*	0.248 (1)	0	0.374 (3)
Na	16*h*	0.025*	0.248 (1)	0	0.374 (3)
O	16*h*	1	0.249 (8)	0	0.126 (2)

Unit cell: a = 5.896 (6) Å, c = 8.416 (6) Å, V = 292.6(8) Å^3, Z = 4.
Isotropic displacement parameters B were fixed to 0.29 Å^2.
*Fixed.

1969; Tomioka and Fujino 1997; Tschauner et al. 2014, 2018; Tomioka et al. 2016). The host rock consists mainly of olivine, enstatite, and shock-vitrified plagioclase ("maskelynite") with accessory ilmenite, titanomagnetite, baddeleyite, merrillite, apatite, and Fe-sulfide. The new phase occurs as lath-shaped, idiomorphic to hypidiomorphic crystallites exhibiting combinations of tetragonal prisms and dipyramids ~200 nm to 1 μm in size. Its mode in the Tenham shock melt vein matrix is ~30 vol% with the remainder composed mainly of a vitrified (Mg,Fe)SiO_3-phase, which exhibits a platy to prismatic habit, indicating a former crystalline state. The bulk matrix composition, estimated by averaging 10 EPMA domain analyses with a defocused beam of 5 μm (Table 1), is close to $(Mg,Fe)_4Si_3O_{10}$, or subequal amounts on a molar basis of $(Mg,Fe)_3Si_2O_7$ (the new silicate) plus (Mg,Fe)SiO_3 (the vitrified phase).

Like in Tenham, the host rock in Suizhou is dominated by olivine, enstatite, and maskelynite. The new phase was observed within the matrix of one shock melt vein along with a (Mg,Fe)SiO_3-clinopyroxene (Fig. 2; second occurrence). The crystal size is generally in the range of 100–800 nm. This occurrence is very similar to that observed in Tenham, except that the coexisting matrix phase is crystalline clinopyroxene instead of vitreous (Mg,Fe)SiO_3. Its mode in the Suizhou shock melt vein matrix is ~40 vol% with the remainder consisting mainly of (Mg,Fe)SiO_3-clinopyroxene. The bulk matrix composition is again close to $(Mg,Fe)_4Si_3O_{10}$ (Table 1). We did not observe (Mg,Fe)SiO_3-glass, but Chen et al. (2004b) reported it and suggested that it might be a vitrified perovskite.

A larger, texturally distinct, ~3 × 7 μm, grain of the new phase was identified at the contact between a ringwoodite clast and vitreous (Mg,Fe)SiO_3 along with spherules of taenite indicating that the vitreous (Mg,Fe)SiO_3 is quenched from a melt (Fig. 3; third occurrence).

Crystal Structure

Rietveld refinement of synchrotron diffraction data for the Tenham material (first occurrence) converged to R_p = 6.8% (R_{wp} = 9.1% with an R_{exp} = 1.8% and an R_F = 8.6% based on the Le Bail–extracted $|F(hkl)|$). Le Bail extraction of $|F(hkl)|$ gave an Rp of 6.5%. Pseudo-Voigt profiles with profile terms U = 0.426, V = −0.048, and W = 0.009, and mixing term n_a = 0.919 were used. The space group of the new phase is $I4_1/amd$, a subgroup of the space group for cubic spinel ($F\bar{3}dm$). It has refined cell parameters of a = 5.896 (6) Å, c = 8.416 (6) Å, V = 292.6(8) Å^3, Z = 4. The cell parameters and composition, as listed in Table 1, lead to a density of 3.59 g cm^{-3}. Site occupancies are given in Table 2 and the calculated structure factors and d-spacings are given in Table S1 in supporting information. Noticeable amounts of Si are found in the octahedral site and vacancies occur in the tetrahedral site. Its empirical formula based on electron microprobe analysis is $(Mg_{0.98}Fe^{2+}_{0.61}Si_{0.23}Al_{0.07}Ca_{0.06}Na_{0.04}Cr^{3+}_{0.01})_{\Sigma=2.00}(Si_{0.88}\square_{0.12})O_4$. Figure 4 shows a representative diffraction pattern of this new phase with contaminant ringwoodite from a clast in the melt matrix.

The second occurrence for the new phase, in Suizhou section SCM1, was characterized using EBSD. Generally, EBSD is not suitable for refining crystal structures or for assessing unit cell parameters. It can, however, be used to test candidate structures. EBSD patterns of the new phase in both Tenham and Suizhou (first and second occurrences) match excellently to the tetragonal structure determined by XRD, with a mean angular deviation <0.40° (Fig. 5).

X-ray diffraction was applied to the third occurrence, where a fragment was extracted from Suizhou section MSN3238/I (Fig. 3). The structure was resolved and refined using the Shelx package (Sheldrick 2008). With anisotropic atomic displacement parameters for all atoms and no constraints, the residual value settled at $R_1(F)$ = 0.0264 for 140 observed reflections [$F_o > 4\sigma(F_o)$] and 14 parameters and at $R_1(F)$ = 0.0363 for all 199 independent reflections. The site occupation factor at the cation sites was allowed to vary (Fe versus Mg and Si versus structural vacancy for the octahedral and tetrahedral sites, respectively) using scattering curves for neutral atoms taken from the *International Tables for Crystallography* (Wilson 1992). The refinement yielded a tetragonal phase in space group $I4_1/amd$, with unit cell parameters: a = 5.934(1) Å, c = 8.349(2) Å, V = 293.99(12) Å^3, Z = 4. These cell

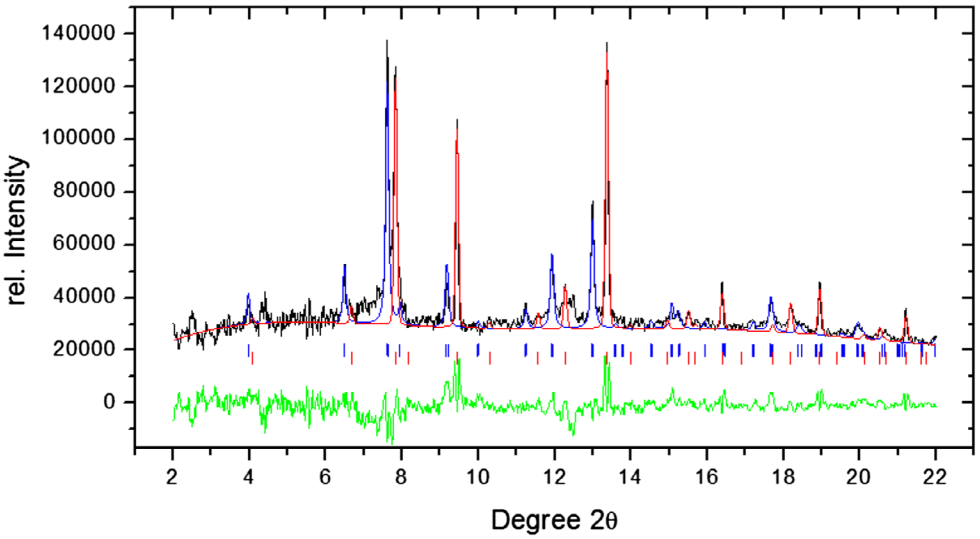

Fig. 4. SXRD powder pattern of SPD in the Tenham shock vein matrix shown in Fig. 1. Blue = phase SPD; red = ringwoodite; green = residual spectrum after fitting the powder pattern to account for SPD and ringwoodite. Tick marks indicate the positions of allowed reflections. Note that no peaks attributable to akimotoite, majorite, or other $(Mg,Fe)SiO_3$ phases were observed. The wavelength was 0.3344 Å. (Color figure can be viewed at wileyonlinelibrary.com.)

parameters and the composition (Table 1) lead to a calculated density of 3.59 g cm^{-3}. The cell parameters and density are generally consistent with those observed for the Tenham sample with ~0.5% larger volume for an occurrence with ~3% higher Fe-content.

DISCUSSION

Crystal-Chemical Considerations

Compositions of the new silicate and associated $(Mg,Fe)SiO_3$ phases are given in Table 1, together with the formulas calculated on the basis of three or four oxygen atoms. All three occurrences of the new phase yield an empirical stoichiometric formula of $(Mg,Fe)_3Si_2O_7$ (equivalent to $[Mg,Fe]_2SiO_4 + [Mg,Fe]SiO_3$). However, the structure refinements clearly show that this phase assumes a spinel structure, equivalent to that of ringwoodite, but with crystal symmetry lowered from the cubic $F\bar{3}dm$ of ringwoodite to its tetragonal subgroup $I4_1/amd$ through a direct group–subgroup mapping. The symmetry reduction is likely the result of the large population of vacancies in the modified spinel that are inevitable for a $Mg_3Si_2O_7$ stoichiometry forced to assume an AB_2O_4-structure. Furthermore, if we keep the observed Mg/Fe ratio and map the tetragonal cell back onto the cubic spinel cell, the unit cell volume of the new spinelloid is intermediate between that of a solid solution of 70 mole% ringwoodite and 30% ahrensite, which is ~8% larger, and the volume of a recently described, totally inverted, pure ringwoodite, which is ~7% smaller (Bindi et al. 2018).

Vacancies in crystal structures are a common indicator of high-temperature conditions. In some cases, however, a high concentration of vacancies is more indicative of high pressure than high temperature. For example, tissintite and the Ca-Eskola molecule in $C2/c$-pyroxenes are high pressure phases whose systematic vacancies stabilize them because they permit the crystal lattice to contract (Ma et al. 2015). The present case is different; although the tetragonal vacancy-rich spinelloid silicate is 5% denser than olivine with the same Mg/Fe ratio, it is also ~8% less dense than the corresponding silicate spinel ringwoodite. Thus, a parameter strongly correlated with the systematic vacancies is the volume expansion of the inverted spinel phase of ~8% relative to stoichiometric ringwoodite. The volume expansion does not imply unusual and unprecedented extension of bonds but is related to the vacancies in this structure.

As noted above, the presence of vacancies does not permit a substantially denser packing for the spinelloid structure. In fact, the spinel structure has only one atomic parameter unfixed by symmetry (the oxygen u-parameter) and this does not allow for much internal relaxation. This structural constraint also holds for the tetragonal structure (Table 2). Hence, the presence of vacancies in the structure of the new phase reflects quench from a high-temperature disordered state at high pressure. At high temperature, cations move between available cation sites in correlation with O-anions. Within the spinel group, γ-Al_2O_3 ($Al_{8/3}O_4$) is an example of a vacancy-stabilized, high-temperature modification (e.g., Sack 2014). The present new silicate is a high temperature stabilized–high pressure phase,

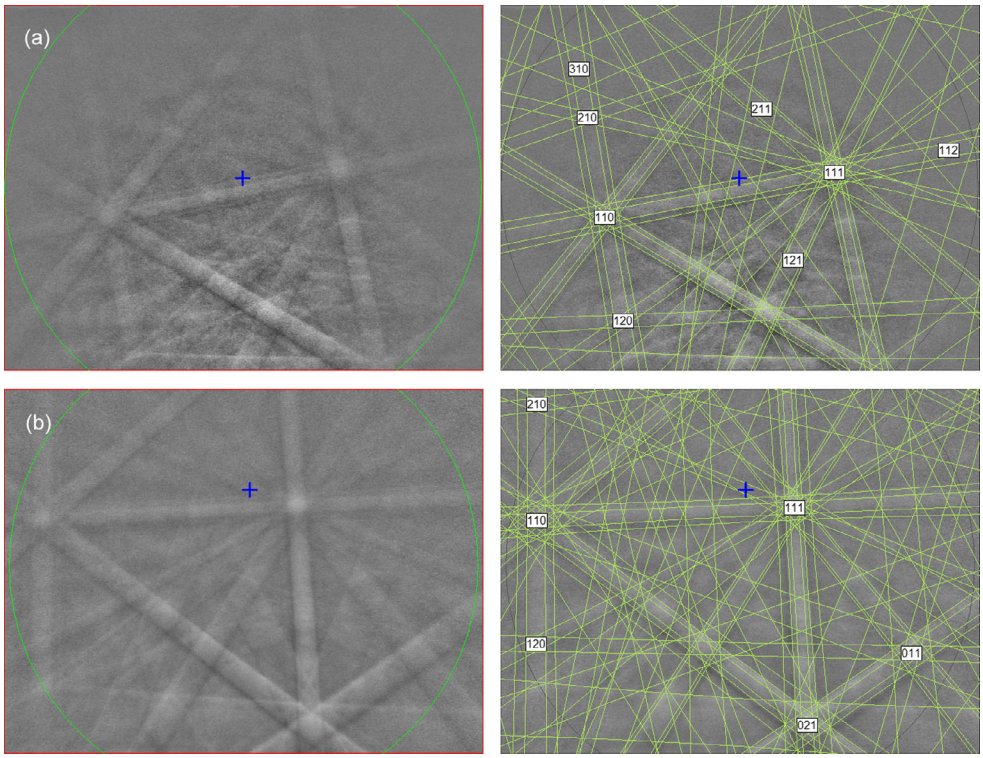

Fig. 5. EBSD patterns of single-crystal spinelloid from (a) Tenham in Fig. 1c and (b) Suizhou section SCM1 in Fig. 2c; both are indexed using the tetragonal structure reported in this paper. The blue cross indicates the center point of the pattern. (Color figure can be viewed at wileyonlinelibrary.com.)

consistent with its occurrence in the fine-grained matrix of shock melt veins (we discuss the third occurrence around converted clasts below).

For the stoichiometric bulk formula of $(Mg,Fe)_3Si_2O_7$ and the tetragonal spinelloid structure, there are two possible mechanisms of substitution:

$$(Mg,Fe)_2SiO_4, + Si_2\square O_4, \rightarrow (Mg,Fe,Si)_2(Si,\square)O_4 + (Mg,Fe)O \quad (1)$$

with a hypothetical, fully inverted, endmember formula of $Si_2\square O_4$, and

$$(Mg,Fe)_2SiO_4, + (Si,\square)_2SiO_4 \rightarrow (Mg,Fe,Si,\square)_2SiO_4 + (Mg,Fe)O \quad (2)$$

with a hypothetical endmember formula of $(Si,\square)_2SiO_4$.

In mechanism 1, with hypothetical endmember formula $Si_2\square O_4$, Si on the octahedral site should induce contraction of the octahedron such that cation-oxygen distances are less than 1.9 Å. Vacancies on the tetrahedral site allow for marked expansion from 1.6–1.7 Å for an occupied site to ~2.2 Å for an empty site. Octahedral Si and tetrahedral vacancies are strictly correlated in this mechanism: Expansion of the T-site permits the contraction of the M-site and vice-versa.

Mechanism 2 can be reconciled with average bond distances only by a high degree of frozen-in disorder. Structure analysis clearly supports mechanism 1. In the absence of occurrences with markedly different composition, we cannot assess the mixing volume relations.

Formation Mechanisms and Implications for Shocked Meteorites

In an earlier study (Tschauner et al. 2014), we used the detection of bridgmanite in shock metamorphized clasts in Tenham shock melt veins to constrain the peak pressure and temperature for these clasts to between 23 and 25 GPa and 2200–2400 K. The shock melt in Tenham is rich in clasts, but its matrix is composed of idiomorphic to hypidiomorphic micrometer-scale crystallites of the inverted spinelloid silicate and an amorphized $(Mg,Fe)SiO_3$ phase. Majoritic garnet, akimotoite, and periclase are rare. However, periclase and majoritic garnet are the expected liquidus phases in the 20–30 GPa pressure regime for peridotite as well as endmember forsterite (e.g., Herzberg and Zhang 1996), but their sparse occurrence within the Tenham and

Suizhou melt matrices indicates that either they were not liquidus phases upon crystallization or that their formation was kinetically inhibited. One may argue that these phases formed but suffered retrograde metamorphism upon release. This, however, conflicts with the observation of bridgmanite, the least metastable high-pressure Mg-silicate, within clasts of the same melt veins in Tenham.

The new spinelloid silicate, which is one of the two dominant phases in the melt vein matrices, has not been reported previously. There are two important implications for its occurrence:

1. Formation of the equilibrium phases, periclase and majorite, was inhibited. In an earlier study, Tomioka et al. (2016) assessed the kinetics of site ordering in majoritic garnets in transformed pyroxene clasts in Tenham, and obtained a lower bound of cooling rates of 10^3 K s^{-1} at pressures in the 17–20 GPa range and a peak temperature of 2200–2300 K. If formation of garnet is kinetically overrun, the quench rate of the examined shock melt veins in Tenham and Suizhou must have been markedly higher than that. Kinetic inhibition of garnet seed formation is unlikely because majoritic garnets do occur, at least in clasts in Tenham melt veins in direct contact with the melt. The rapid quench regime is succeeded by slow conductive, nearly adiabatic, cooling at temperatures below $\sim$1200 K, estimated based on the lower bound for cation ordering in majorite (Tomioka et al. 2016; see their fig. 4), where temperature differences between melt veins and surrounding shock-heated bedrock become sufficiently small. Furthermore, the rapid quench regime has to occur at sufficiently high pressure (in the GPa range at $\sim$400 K, which would be close to the expected Hugoniot of a nonporous chondrite; Scott et al. 1992) to prevent back-conversion of high-pressure phases such as bridgmanite, akimotoite, or the present spinelloid silicate (e.g., Tschauner et al. 2014) and followed by slower cooling at sufficiently low temperature. Thus, the onset of slow conductive cooling in the melt and small clasts occurred at even lower temperatures, below 1000 K in the examined melt veins (Tschauner et al. 2014). The observation of the inverted silicate-spinel in the melt matrix coincides with the observation of bridgmanite in embedded clasts. Hence, the peak shock pressure of the melt must have been in the 24–27 GPa regime, as already assessed by Tschauner et al. (2014), and a temperature of 2700–2800 K or higher (the lower pressure polymorphs like ringwoodite only occur in cooler regions at the melt vein rim or in clasts). Thus, the quench rate was at least twice as high as assessed by Tomioka et al. (2016): 5×10^3 K s^{-1}. Overall, the present model of rapid quench at high pressure is consistent with previous assessments of rapid, high-pressure cooling paths and regimes in shock melt veins in L6 chondrites (Tschauner et al. 2014; Tomioka et al. 2016). We note that cooling is accelerated by conversion of clasts in the melt veins. Quench rates in shock melt veins depend on the diameter of the melt vein which is $\sim$100 (Suizhou) and 500 μm (Tenham) in the plane of the thin section and at least 30 μm perpendicular to the plane of the section because both veins cut through the entire thickness of the section (Figs. 1–3). Much thinner or thicker veins would be expected to experience much different cooling histories. Finally, we note that the implied high cooling rates over distances of tens to 100 μm are equivalent to velocities in the 1–10 m s^{-1} range or higher. Such cooling rates are in the range of shock-induced turbulences in heterogeneous shocked melts, indications of which have been found in shocked silicate-metal melts (Tschauner et al. 2005) and which also match the apparent growth rates of the silicate-spinelloid wadsleyite in a shock experiment (Tschauner et al. 2009). Hence, crystal growth within shock-generated melt may be controlled by mass transport through turbulent mixing rather than diffusion.
2. Under liquidus conditions at 24–27 GPa, the new phase assumes a dynamically disordered, vacancy-rich spinelloid structure which, upon the rapid quench of shock melt veins, is conserved as the partially inverted, vacancy-rich spinelloid silicate that we observe. In static high-pressure experiments, this phase breaks down at the liquidus boundary to form majoritic garnet and periclase, the observed liquidus phases:

$$Mg_3Si_2O_7(\text{spinelloid}) \rightarrow 2MgSiO_3(\text{majorite}) + MgO\ (\text{periclase}) \quad (3)$$

The vacancy-stabilized spinelloid silicate forms at the dynamic liquidus because rapid quench from the melt state prevents the formation of garnet and periclase. Our observation of the vacancy stabilized spinelloid phase and pyroxene instead of a glass is consistent with experimental indications that at least $MgSiO_3$-glass is not a silicate network at high pressure and approaches the structure of akimotoite around 30 GPa (Kono et al. 2018). The occurrence of $(Mg,Fe)SiO_3$-clinopyroxene in Suizhou melt matrices (second occurrence) rather than the vitrified $(Mg,Fe)SiO_3$ phase observed in Tenham implies a longer low-temperature annealing regime for the former. We suggest that the amorphized metasilicate in Tenham was in fact a high-pressure clinopyroxene (Yang et al. 1999) that vitrified

upon pressure release. We can clearly rule out a metastable phase assemblage of akimotoite plus garnet as a significant component in the shock melt matrices. Isolated akimotoite crystals in the matrix are rare and readily explained as break-off from entrained clasts. Similarly, rare garnet is observed as isolated, larger crystallites with compositions different from the bulk matrix; these also represent transformed clasts. Overall, the observed shock melt matrix parageneses of Tenham and Suizhou reflect metastable crystallization (i.e., the stable liquidus phase(s) failed to nucleate) of a vacancy-rich spinelloid and clinopyroxene with or without subsequent vitrification of the clinopyroxene.

CONCLUDING REMARKS

A high-pressure spinelloid silicate, $(Mg,Fe,Si)_2(Si,\square)O_4$, was discovered within shock melt veins in the highly shocked Tenham and Suizhou L6 ordinary chondrites. Unlike known silicate-spinels, this new phase exhibits inversion of Si along with intrinsic vacancies and reduction of symmetry. Inversion in naturally occurring silicate-spinels is a new observation, so far reported only in this and in one other recent study (Bindi et al. 2018). It carries the potential for supporting constraints on high-pressure geothermometry and kinetic effects. Together with a $(Mg,Fe)SiO_3$ phase, this new silicate forms the bulk of the matrix of melt veins in Tenham and Suizhou. Majoritic garnet and akimotoite occur only as rare isolated grains.

Putting the observed shock melt matrix phases in context with the equilibrium liquidus phases in the peridotite phase diagram, we estimate high-pressure quench rates higher than 5×10^3 K s^{-1} followed by a low-temperature annealing regime that continues to full pressure release. We argue that the vacancy-rich, inverted spinel structure reflects features of the melt structure of primitive chondritic melts in the 24–27 GPa pressure regime.

Acknowledgments—SEM, EBSD, and EPMA analyses were carried out at the Caltech GPS Division Analytical Facility, which is supported, in part, by NSF Grants EAR-0318518 and DMR-0080065. Raman analysis was performed in the Rossman Lab at Caltech. Synchrotron diffraction was carried out at the 13-IDD beamline of the Advanced Photon Source. Use of the Advanced Photon Source, an Office of Science User Facility operated for the U.S. Department of Energy (DOE) Office of Science by Argonne National Laboratory, was supported by the U.S. DOE under contract no. DE-AC02-06CH11357. Suizhou section SCM1 was provided to C. M. by Prof. Renjing Wang at China University of Geosciences (Wuhan). We thank Axel Wittmann and AE Wolf Uwe Reimold for their constructive reviews.

Editorial Handling—Dr. W. Uwe Reimold

REFERENCES

Armstrong J. T. 1995. CITZAF: A package of correction programs for the quantitative electron microbeam X-ray analysis of thick polished materials, thin films, and particles. *Microbeam Analysis* 4:177–200.

Bindi L. and Xie X. 2018. Shenzhuangite, $NiFeS_2$, the Ni-analogue of chalcopyrite from the Suizhou L6 chondrite. *European Journal of Mineralogy* 30:165–169.

Bindi L., Chen M., and Xie X. 2017. Discovery of the Fe-analogue of akimotoite from the shocked Suizhou L6 chondrite. *Scientific Reports* 7:42674.

Bindi L., Griffin W. L., Panero W., Sirotkina E. A., Bobrov A., and Irifune T. 2018. Synthesis of inverse ringwoodite sheds light on the subduction history of Tibetan ophiolites. *Scientific Reports* 8:5457.

Binns R. A., Davis R. J., and Reed S. J. B. 1969. Ringwoodite, natural $(Mg, Fe)_2SiO_4$ Spinel group in the Tenham meteorite. *Nature* 221:943–944.

Chen M., Xie X., Wang D., and Wang S. 2002. Metal-troilite-magnetite assemblage in shock veins of Sixiangkou meteorite. *Geochmica et Cosmochimica Acta* 66: 3143–3149.

Chen M., El Goresy A., Frost D., and Gillet P. 2004a. Melting experiments of a chondritic meteorite between 16 and 25 GPa: Implication for Na/K fractionation in a primitive chondritic Earth's mantle. *European Journal of Mineralogy* 16:203–211.

Chen M., Xie X., and El Goresy A. 2004b. A shock-produced $(Mg, Fe)SiO_3$ glass in the Suizhou meteorite. *Meteoritics & Planetary Science* 39:1797–1808.

Dera P., Zhuravlev K., Prakapenka V., Rivers M. L., Finkelstein G. J., Grubor-Urosevic O., Tschauner O., Clark S. M., and Downs R. T. 2013. High pressure single-crystal micro X-ray diffraction analysis with GSE_ADA/RSV software. *High Pressure Research* 33:466–484.

Fabrichnaya O. B. 1995. Thermodynamic data for phases in the FeO-MgO-SiO_2 system and phase-relations in the mantle transition zone. *Physics and Chemistry of Minerals* 22:323–332.

Ferroir T., Beck P., Van de Moortèle B., Bohn M., Reynard B., Simionovici A., El Goresy A., and Gillet P. 2008. Akimotoite in the Tenham meteorite: Crystal chemistry and high-pressure transformation mechanisms. *Earth and Planetary Science Letters* 275:26–31.

Gillet P., Chen M., Dubrovinsky L., and El Goresy A. 2000. Natural $NaAlSi_3O_8$-hollandite in the shocked Sixiangkou meteorite. *Science* 287:1633–1636.

Herzberg C. and Zhang J. 1996. Melting experiments on anhydrous peridotite KLB-1: Compositions of magmas in the upper mantle and transition zone. *Journal of Geophysical Research: Solid Earth* 101:8271–8295.

Hu J. and Sharp T. G. 2017. Back-transformation of high-pressure minerals in shocked chondrites: Low-pressure mineral evidence for strong shock. *Geochimica et Cosmochimica Acta* 215:277–294.

Jilly-Rehak C. E., Huss G. R., Bonal L., and Twelker E. 2016. Petrography and classification of NWA 7402: A new

sulfide-rich unequilibrated ordinary chondrite. *Chemie der Erde* 76:111–136.

Kono Y., Shibazaki Y., Kenney-Benson C., Wang Y., and Shen G. 2018. Pressure-induced structural change in $MgSiO_3$ glass at pressures near the Earth's core-mantle boundary. *Proceedings of the National Academy of Sciences of the United States of America* 115:1742–1747.

Ma C. and Rossman G. R. 2008. Barioperovskite, $BaTiO_3$, a new mineral from the Benitoite Mine, California. *American Mineralogist* 93:154–157.

Ma C., Tshauner O., Beckett J. R., Liu Y., Rossman G. R., Zhuravlev K., Prakapenka V., Dera P., and Taylor L. A. 2015. Tissintite, (Ca, Na,□)$AlSi_2O_6$, a highly defective, shock-induced, high-pressure clinopyroxene in the Tissint martian meteorite. *Earth and Planetary Science Letters* 422:194–205.

Ma C., Tschauner O., Becket J. R., Liu Y., Rossman G. R., Sinogeikin S. V., Smith J. S., and Taylor L. A. 2016. Ahrensite, γ-Fe_2SiO_4, a new shock-metamorphic mineral from the Tissint meteorite: Implications for the Tissint shock event on Mars. *Geochimica et Cosmochimica Acta* 184:240–256.

Ma C., Tschauner O., Beckett J. R., Rossman G. R., Prescher C., Prakapenke V. B., Bechtel H. A., and McDowell A. 2018. Liebermannite, $KAlSi_3O_8$, a new shock-metamorphic, high-pressure mineral from the Zagami Martian meteorite. *Meteoritics & Planetary Science* 53:50–61.

Mori H. 1994. Shock-induced phase transformations on the Earth and planetary materials. *Journal of the Mineralogical Society of Japan* 23:171–178.

Mosenfelder J. L., Asimow P. D., Frost D. J., Rubie D. C., and Ahrens T. J. 2009. The $MgSiO_3$ system at high pressure: Thermodynamic properties of perovskite, postperovskite, and melt from global inversion of shock and static compression data. *Journal of Geophysical Research* 114:B01203.

Oxford Diffraction. 2006. CrysAlis *RED (Version 1.171.31.2) and ABSPACK in* CrysAlis *RED*. Abingdon, UK: Oxford Diffraction Ltd

Prescher C., and Prakapenka V. B. 2015. *DIOPTAS*: a program for reduction of two-dimensional X-ray diffraction data and data exploration. *High Pressure Research* 35:223–230.

Price G. D., Putnis A., Agrell S. O., and Smith D. G. W. 1983. Wadsleyite, natural β-(Mg, Fe)$2SiO_4$ from the Peace river meteorite. *Canadian Mineralogist* 21:29–35.

Sack R. O. 2014. $MgAl_2O_4$–$Al_{8/3}O_4$ spinels: Formulation and calibration of the low-pressure thermodynamics of mixing. *American Journal of Science* 314:858–877.

Scott E. R. D., Keil K., and Stöffler D. 1992. Shock metamorphism of carbonaceous chondrites. *Geochimica et Cosmochimica Acta* 56:4281–4293.

Sears D. W., Grossman J. N., Melcher C. L., Ross L. M., and Mills A. A. 1980. Measuring metamorphic history of unequilibrated ordinary chondrites. *Nature* 287:791–795.

Sharp T. G. and DeCarli P. S. 2006. Shock effects in meteorites. In *Meteorites and the early solar system II*, edited by Lauretta D. S. and McSween H. Y. Tucson, Arizona: The University of Arizona Press. pp. 653–677.

Sharp T. G., Lingemann C. M., Dupas C., and Stöffler D. 1997. Natural occurrence of $MgSiO_3$-ilmenite and evidence for $MgSiO_3$-perovskite in a shocked L chondrite. *Science* 277:352–355.

Sheldrick G. M. 2008. A short history of SHELX. *Acta Crystallographica Section A* 64:112–122.

Smith J. V. and Mason B. 1970. Pyroxene-garnet transformation in Coorara meteorite. *Science* 168:832–833.

Stöffler D. 1997. Minerals in the deep Earth: A message from the asteroid belt. *Science* 278:1576–1577.

Stöffler D., Keil K., and Scott E. R. D. 1991. Shock metamorphism of ordinary chondrites. *Geochimica et Cosmochimica Acta* 55:3845–3867.

Stöffler D., Hamann C., and Metzler K. 2018. Shock metamorphism of planetary silicate rocks and sediments: Proposal for an updated classification system. *Meteoritics & Planetary Science* 53:5–49.

Tomioka N. and Fujino K. 1997. Natural (Mg, Fe)SiO_3-ilmenite and -perovskite in the Tenham meteorite. *Science* 277:1084–1086.

Tomioka N. and Fujino K. 1999. Akimotoite, (Mg, Fe)SiO_3, a new silicate mineral of the ilmenite group in the Tenham chondrite. *American Mineralogist* 84:267–271.

Tomioka N., Miyahara M., and Ito M. 2016. Discovery of natural $MgSiO_3$ tetragonal garnet in a shocked chondritic meteorite. *Science Advances* 2:e1501725.

Tschauner O., Willis M. J., Asimow P. D., and Ahrens T. J. 2005. Effective liquid metal-silicate mixing upon shock by power-law droplet size scaling in Richtmyer-Meshkov like perturbations. *LPI Contributions* 1234:1802.

Tschauner O., Asimow P. D., Kostandova N., Ahrens T. J., Ma C., Sinogeikin S., Liu Z., Fakra S., and Tamura N. 2009. Ultrafast growth of wadsleyite in shock-produced melts and its implications for early solar system impact processes. *Proceedings of the National Academy of Sciences of the United States of America* 106: 13,691–13,695.

Tschauner O., Ma C., Beckett J. R., Prescher C., Prakapenka V. B., and Rossman G. R. 2014. Discovery of bridgmanite, the most abundant mineral in Earth, in a shocked meteorite. *Science* 346:1100–1102.

Tschauner O., Ma C., Prescher C., and Prakapenka V. 2018. Structure analysis and conditions of formation of akimotoite in the Tenham chondrite. *Meteoritics & Planetary Science* 53:62–74.

Van Schmus W. R. and Wood J. A. 1967. A chemical-petrologic classification for the chondritic meteorites. *Geochimica et Cosmochimica Acta* 31:747–765.

Walton E. L., Sharp T. G., Hu J., and Filiberto J. 2014. Heterogeneous mineral assemblages in Martian meteorite Tissint as a result of a recent small impact event on Mars. *Geochimica et Cosmochimica Acta* 140:334–348.

Wang D. and Rubin A. E. 1987. Petrology of nine ordinary chondrite falls from China. *Meteoritics* 22:97–104.

Wilson A. J. C. Ed. 1992. *International tables for crystallography, Volume C: Mathematical, physical and chemical tables*. Dordrecht: Kluwer Academic.

Xie X. and Chen M. 2016. *Suizhou meteorite: Mineralogy and shock metamorphism*. Berlin: Springer-Verlag and Guangdong Science & Technology Press Co., Ltd. 258 p.

Xie X., Chen M., and Wang D. 2001. Shock-related mineralogical features and P-T history of the Suizhou L6 chondrite. *European Journal of Mineralogy* 13:1177–1190.

Yang H., Finger L. W., Conrad P. G., Prewitt C. T., and Hazen R. M. 1999. A new pyroxene structure at high pressure: Single-crystal X-ray and Raman study of the *Pbcn*-$P2_1cn$ phase transition in protopyroxene. *American Mineralogist* 84:245–256.

SUPPORTING INFORMATION

Additional supporting information may be found in the online version of this article:.

Table S1. List of observed and calculated factor moduli of Tenham occurrence.

Figure S1. Optical image of Tenham section USNM 7703 showing the black SPD-bearing shock melt vein.

Figure S2. Optical image of Suizhou section SCM1 showing the SPD-bearing shock melt vein.

Figure S3. Monte Carlo electron trajectory simulation of the interaction volume in the spinelloid silicate (SPD) at 10 keV as blue traces. The beam electron trajectories emerging as backscattered electrons are shown as red traces.